

## High-resolution whole-brain DCE-MRI using constrained reconstruction: Prospective clinical evaluation in brain tumor patients

Yi Guo, R. Marc Lebel, Yinghua Zhu, Sajan Goud Lingala, Mark S. Shiroishi, Meng Law, and Krishna Nayak

Citation: *Medical Physics* **43**, 2013 (2016); doi: 10.1118/1.4944736

View online: <http://dx.doi.org/10.1118/1.4944736>

View Table of Contents: <http://scitation.aip.org/content/aapm/journal/medphys/43/5?ver=pdfcov>

Published by the [American Association of Physicists in Medicine](http://www.aapm.org/)

### Articles you may be interested in

[A localized Richardson–Lucy algorithm for fiber orientation estimation in high angular resolution diffusion imaging](#)

*Med. Phys.* **42**, 2524 (2015); 10.1118/1.4917082

[Magnetoacoustic tomography with magnetic induction for high-resolution bioimpedance imaging through vector source reconstruction under the static field of MRI magnet](#)

*Med. Phys.* **41**, 022902 (2014); 10.1118/1.4862836

[DCE-MRI defined subvolumes of a brain metastatic lesion by principle component analysis and fuzzy-c-means clustering for response assessment of radiation therapy](#)

*Med. Phys.* **41**, 011708 (2014); 10.1118/1.4842556

[Diffusion tensor imaging using a high-temperature superconducting resonator in a 3 T magnetic resonance imaging for a spontaneous rat brain tumor](#)

*Appl. Phys. Lett.* **102**, 063701 (2013); 10.1063/1.4790115

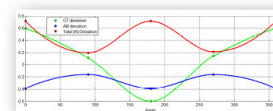
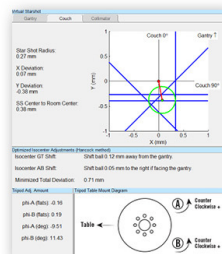
[Feasibility of high temporal resolution breast DCE-MRI using compressed sensing theory](#)

*Med. Phys.* **37**, 4971 (2010); 10.1118/1.3483094

**Achieve  
Sub Millimeter  
Accuracy**



- Fast and accurate EPID-based measurement of isocenter position
- Characterization of gantry, couch, and collimator rotation
- Calculates optimization of couch axis automatically
- Compatible with MLC, jaw, or cone based fields of all sizes



New - Eliminate your need for films, and increase your accuracy by using the all new Virtual Starshot, reconstructed using a set of Winston-Lutz images! US Patent 9,192,784

# High-resolution whole-brain DCE-MRI using constrained reconstruction: Prospective clinical evaluation in brain tumor patients

Yi Guo<sup>a)</sup>

Ming Hsieh Department of Electrical Engineering, Viterbi School of Engineering, University of Southern California, Los Angeles, California 90089

R. Marc Lebel

GE Healthcare, Calgary, Alberta AB T2P 1G1, Canada

Yinghua Zhu and Sajan Goud Lingala

Ming Hsieh Department of Electrical Engineering, Viterbi School of Engineering, University of Southern California, Los Angeles, California 90089

Mark S. Shiroishi and Meng Law

Department of Radiology, Keck School of Medicine, University of Southern California, Los Angeles, California 90033

Krishna Nayak

Ming Hsieh Department of Electrical Engineering, Viterbi School of Engineering, University of Southern California, Los Angeles, California 90089

(Received 29 September 2015; revised 10 February 2016; accepted for publication 9 March 2016; published 4 April 2016)

**Purpose:** To clinically evaluate a highly accelerated T1-weighted dynamic contrast-enhanced (DCE) MRI technique that provides high spatial resolution and whole-brain coverage via undersampling and constrained reconstruction with multiple sparsity constraints.

**Methods:** Conventional (rate-2 SENSE) and experimental DCE-MRI (rate-30) scans were performed 20 minutes apart in 15 brain tumor patients. The conventional clinical DCE-MRI had voxel dimensions  $0.9 \times 1.3 \times 7.0 \text{ mm}^3$ , FOV  $22 \times 22 \times 4.2 \text{ cm}^3$ , and the experimental DCE-MRI had voxel dimensions  $0.9 \times 0.9 \times 1.9 \text{ mm}^3$ , and broader coverage  $22 \times 22 \times 19 \text{ cm}^3$ . Temporal resolution was 5 s for both protocols. Time-resolved images and blood–brain barrier permeability maps were qualitatively evaluated by two radiologists.

**Results:** The experimental DCE-MRI scans showed no loss of qualitative information in any of the cases, while achieving substantially higher spatial resolution and whole-brain spatial coverage. Average qualitative scores (from 0 to 3) were 2.1 for the experimental scans and 1.1 for the conventional clinical scans.

**Conclusions:** The proposed DCE-MRI approach provides clinically superior image quality with higher spatial resolution and coverage than currently available approaches. These advantages may allow comprehensive permeability mapping in the brain, which is especially valuable in the setting of large lesions or multiple lesions spread throughout the brain. © 2016 Author(s). All article content, except where otherwise noted, is licensed under a Creative Commons Attribution 3.0 Unported License. [<http://dx.doi.org/10.1118/1.4944736>]

Key words: DCE-MRI, compressed sensing, constrained reconstruction, clinical evaluation

## 1. INTRODUCTION

T1-weighted dynamic contrast-enhanced (DCE)-MRI is a valuable albeit still evolving technique for mapping the spatial distribution of brain vascular parameters such as perfusion, permeability, and blood volume.<sup>1,2</sup> It employs serial T1-weighted imaging before, during, and after a bolus injection of a gadolinium-based contrast agent (GBCA). Changes in GBCA concentration are derived from changes in signal intensity, then regressed to quantify pharmacokinetic (PK) parameters such as  $K^{\text{trans}}$  (volume transfer constant),  $v_p$  (fractional plasma volume), and  $v_e$  (fractional extravascular extracellular space volume).<sup>3,4</sup> DCE-MRI is used for quantitative assessment of brain tumors,<sup>5–7</sup> multiple sclerosis lesions,<sup>8</sup>

and Alzheimer's disease,<sup>9</sup> and other neurological disorders that involve blood–brain barrier (BBB) disruption. DCE-MRI is also used in clinical oncologic imaging for assessment of breast<sup>10</sup> and prostate<sup>11</sup> cancer. In brain tumor evaluation, BBB permeability is typically characterized by  $K^{\text{trans}}$ .<sup>4</sup> While its interpretation may be complex, with some dependency on blood flow,  $K^{\text{trans}}$  correlates with tumor severity and may be a useful biomarker for monitoring therapeutic response and outcome.<sup>4,8,12–15</sup>

Despite its usefulness, conventional clinical DCE-MRI is limited by suboptimal image acquisition that results in low spatial/temporal resolution and insufficient spatial coverage. Low temporal resolution has also been linked to poor reproducibility of PK parameters.<sup>16</sup> A typical clinical DCE

scan provides 2–30 s temporal resolution to detect signal intensity changes resulting from contrast agent perfusion.<sup>1,17</sup> As a result, the in-plane voxel dimensions usually exceed 1 mm<sup>2</sup> and the slices are often greater than 5 mm thick. The spatial coverage is often inadequate to cover the known pathology, such as in the setting of multiple metastatic lesions.

Recently, compressed sensing (CS) theory has inspired a wide array of new data acquisition and constrained reconstruction strategies that aim to reconstruct images from sparsely undersampled data.<sup>18</sup> CS is particularly well suited for dynamic imaging, which can exploit the redundancy of information in the temporal dimension, either through dictionary-learning<sup>19,20</sup> or high-pass filtering.<sup>21,22</sup> A combination of parallel imaging<sup>23</sup> (PI) and CS has been shown to greatly accelerate the data acquisition, while achieving significantly higher spatiotemporal resolution and large spatial coverage with only slight image quality penalties.<sup>24–26</sup>

Several groups, including ours, have employed PI-CS techniques to improve DCE imaging. Zhang *et al.*<sup>27</sup> employed a locally low-rank constraint in combination with parallel imaging to achieve up to 19× acceleration rate in pediatric patients. Wang *et al.*<sup>28</sup> used a reference image-based compressed sensing and achieved acceleration factor of 10× without degrading spatial resolution. Feng *et al.*<sup>26</sup> used compressed sensing, parallel imaging, and golden-angle radial sampling to achieve fast and flexible DCE-MRI. Rosenkrantz *et al.*<sup>17</sup> examined 20 prostate cancer patients using a similar scheme to evaluate the results from constrained reconstruction against conventional DCE-MRI.

Several groups have also utilized undersampling and constrained reconstruction techniques to accelerate contrast-enhanced (CE) magnetic resonance angiography (MRA). CE-MRA is particularly amenable to this approach because subtraction angiograms are sparse in the image domain. Barger *et al.*<sup>29</sup> used undersampled 3D projection reconstruction trajectories and a “tornado” view-sharing scheme to achieve isotropic resolution, broad coverage, and 4 s temporal resolution. The typical aliasing when using undersampling is mitigated by the high-contrast properties in MRA. Haider *et al.*<sup>30</sup> used a Cartesian radial technique in combination with 2D SENSE, partial Fourier, and view-sharing to achieve 1–2 mm isotropic resolution and subsecond temporal resolution. With emerging CS techniques, Trzasko *et al.*<sup>31</sup> demonstrated reduced noise and artifacts level in Cartesian radial sampling MRA by utilizing a sparsity-driven nonconvex CS method, and Lee *et al.*<sup>32</sup> achieved 1-mm isotropic resolution, 1.1 s frame rate (corresponding to an acceleration factor of >100) with a CS based GraDeS algorithm. In CE-MRA, high spatiotemporal resolution and broad coverage are achieved by exploiting high image contrast and a high degree of image domain sparsity.

Accelerating DCE-MRI for the purpose of pharmacokinetic modeling is more challenging than for CE-MRA since the reconstruction is not spatially sparse and PK modeling is performed based on every signal containing voxel. Furthermore, reconstruction fidelity must be very high for accurate modeling whereas moderate error in visually assessed angiograms is often tolerable. Finally, the dynamic range of contrast-induced

signal change is smaller in tissue than in vessels, enabling subtle compression artifacts to translate into noticeable errors in tissue parameters. The novelty of our proposed approach is that multiple sparsity constraints are employed in different sparse transform domains, each with low weight,<sup>33</sup> mitigating biased artifacts producing from one heavy constraint. We have been able to achieve the highest acceleration rate reported in the literature to date, 36×, with excellent image quality. This enabled near isotropic voxel dimensions with whole-brain coverage for DCE-MRI.

Despite the promise of PI-CS methods, these techniques are poorly validated. Most validation has been done by retrospectively discarding data from fully sampled data sets or using phantom simulation. Both approaches provided ground truth, but are imperfect due to unrealistic data acquisition or anatomical features. Prospectively undersampled studies demonstrate the potential of the method, but lack ground truth images and have not been well validated. In this work, we present the first, to the best of our knowledge, prospective clinical evaluation of accelerated DCE-MRI using constrained reconstruction in brain tumor patients.

## 2. MATERIALS AND METHODS

### 2.A. High-resolution whole-brain DCE-MRI

The experimental DCE-MRI scan was based on a conventional Cartesian T1-weighted 3D spoiled fast gradient (SPGR) echo sequence. The flip angle was 15°, TE was 2 ms, and TR was 6 ms. The phase encoding order was altered to follow a Cartesian-grid golden-angle radial scheme,<sup>34–36</sup> which acquired  $k_y$ – $k_z$  phase encodes following golden-angle rotating radial spokes. The frequency encoding direction  $k_x$  was fully sampled. Cartesian SPGR scans with flip angles of 2°, 5°, and 10° were performed sequentially for DESPOT1 (Ref. 37) T1 mapping prior to both the conventional and experimental DCE scans.

The Cartesian golden-angle radial sampling scheme provides incoherent  $k$ -space sampling, even at very high acceleration rates, where only a few spokes are presented within one time frame.<sup>17,26</sup> This approach provides comparable image quality as Poisson-ellipse sampling, which has been used in similar  $l_1$ -based reconstruction.<sup>36</sup> All samples fall on a 3DFT Cartesian grid, therefore the fast Fourier transform (FFT) operator can be directly applied. We have implemented this sampling scheme on a clinical scanner (3T GE Signa Excite HDx scanner), where the phase encode order table can be generated in response to operator input. The implementation is straightforward, since no additional modification of the existing gradient waveform is needed.<sup>38</sup>

The undersampled raw data were reconstructed using a sparse SENSE reconstruction scheme that utilizes multiple  $l_1$ -norm constraints with very low weights, as described in Ref. 33. These sparsity penalties were chosen based on expected spatial and temporal characteristics of DCE-MRI images. Reconstruction involved solving the minimization problem in Eq. (1), where the final image,  $x$ , remains consistent with the acquired data,  $y$ , yet is sparse in the temporal finite

difference ( $V$ ) domain, the spatial “db2” wavelet domain ( $\Psi$ ), and the spatial total variation (TV) domain. The image is related to the acquired data using known coil sensitivities ( $S$ ) and the undersampling Fourier transform  $F_u$ . Coil sensitivity maps were generated by computing a density compensated average of all  $k$ -space data acquired at all DCE time points. This resulted in high-SNR time-averaged 3D  $k$ -space dataset that was fully sampled. Individual coil maps were then computed in the standard way, by dividing each individual coil image by the root sum-of-squares image,<sup>23</sup>

$$x = \underset{x}{\operatorname{argmin}} \|y - F_u S x\|_2^2 + \lambda_1 \|Vx\|_1 + \lambda_2 \|TVx\|_1 + \lambda_3 \|\Psi x\|_1. \quad (1)$$

This optimization problem is solved by an efficient augmented-Lagrangian method, alternating direction method of multipliers (ADMM), which performs variable splitting twice.<sup>39</sup> This algorithm is one of the many state-of-the-art algorithms to solve these  $l_1$ -constrained minimization problems.<sup>18,24</sup> This particular algorithm was chosen because it provides fast convergence.<sup>39-41</sup> Reconstruction was implemented in MATLAB (Mathworks, Natick, MA) and run on a Linux workstation (24 core 2.5 GHz, 128GB RAM). A detailed description of this algorithm is included in Appendix A.

In this study, regularization penalties were chosen empirically based on retrospective studies. A fully sampled DCE data set was retrospectively undersampled at the same acceleration rate as our prospective data, then repeatedly reconstructed with a range of constraint penalties. Normalized root Mean squared error (nRMSE) was calculated between the fully sampled and reconstructed data sets. Penalties were chosen to maintain near-minimal nRMSE, yet provide traction during reconstruction—essentially locating the corner point of the  $l$ -curve.<sup>42</sup> We employed penalties of 0.01, 0.0001, and 0.0001 for temporal finite difference, spatial TV, and spatial wavelet, respectively, for all subsequent reconstructions. In retrospective studies, we found that reconstruction converged well within 100 iterations. We therefore allowed a maximum of 100 iterations in this prospective study, to provide control of the maximum reconstruction time.

## 2.B. Experimental methods

Fifteen brain tumor patients were recruited from three of our affiliated sites. Informed consent was obtained from patients prior to MRI scan. Our Institutional Review Board approved this study and all procedures.

MRI scans were performed on a clinical 3T scanner (HDxt, GE Healthcare, Waukesha, WI) with an eight-channel head coil. Two DCE scans were performed: a standard (“conventional”) scan using the vendor supplied sequence and our highly accelerated (“experimental”) scan. Both DCE acquisitions used a 3D SPGR sequence. Prior to each scan, T1 maps were acquired using variable flip angle DESPOT1 method.<sup>37</sup> The standard clinical postcontrast T1 weighted scans (Coronal T1-weighted FSPGR sequence, 1.0 mm<sup>3</sup> isotropic resolution, 22 × 22 × 20 cm<sup>3</sup> FOV) were used as the reference for lesion identification.<sup>43,44</sup>

TABLE I. Comprehensive MRI protocol for a brain tumor patient in our study with a conventional-then-experimental DCE MRI order. Conventional and experimental DCE scans are in bold and separated by roughly 20 min. The conventional and experimental scans were reversed for the last two patients.

Duration (min:s)	Sequence
1:00	Localization and SENSE calibration
4:00	Precontrast axial T1w FSPGR
5:00	Precontrast axial T2w FSE
5:00	Precontrast axial FLAIR
0:45	T1 mapping
4:08	Conventional DCE
15:00	Diffusion tensor imaging
0:45	T1 mapping
5:29	<b>Experimental DCE</b>
2:00	Postcontrast axial T1w FSPGR
3:00	Postcontrast coronal T1w FSPGR
<50:00	Total

Table I shows the conventional-then-experimental imaging protocol, which required less than 50 min. The contrast agent, Gadobenate dimeglumine (MultiHance Bracco, Inc.) was administered with a dose of 0.05 mmol/kg, followed by a 20 ml saline flush in the left arm by intravenous injection for each scan (this results in a total of 0.1 mmol/kg which would be the standard dose for a DCE MRI with contrast). The two DCE scans were separated by approximately 20 min, resulting in residual GBCA present in the second scan. This residue results in underestimation of  $K^{\text{trans}}$  values for the second scan, as explained in Appendix B.

Conventional-then-experimental protocols were performed in the first 13 patients; for the last two cases, we switched the order of the conventional and experimental scans and created an experimental-then-conventional protocol. This was for the purpose of verifying that  $K^{\text{trans}}$  underestimation in the second scan was due to the scan order and residual GBCA and not due to the imaging methods.

Table II lists acquisition parameters for the two DCE scans. The experimental scan achieved much smaller voxel dimensions and whole-brain coverage, while maintaining the same temporal resolution as the conventional scan. A net acceleration factor of 30× was achieved. All 15 brain scans had the same field-of-view, matrix size, voxel dimensions, scan time, and phase encode order. K-t space was undersampled in the exact same fashion for all subjects. The injection delay for the experimental method was 60 s, compared to 20 s for the conventional method, in order to allow time for fully sampling of 25% of phase encodes prior to contrast arrival.

## 2.C. Comparisons/evaluation

The conventional and experimental DCE-MRI scans were registered based on the peak-contrast images using MATLAB image registration toolbox. As the experimental scan had whole-brain coverage, slices within the FOV of the conventional scan were located by registration. For fair evaluation, three adjacent

TABLE II. Scan parameters for the standard conventional and experimental high-resolution whole-brain DCE MRI scans. The experimented scan slice thickness is less than one third of that of conventional scan, and the slice number is 17× greater than that of conventional scan. This enables a whole-brain near-isotropic coverage of the experimental scan while keeping the same temporal resolution.

	Conventional	Experimental
TR/TE (ms)	6/2	6/2
Flip angle (deg)	15	15
Matrix size	256×186×6	256×256×100
FOV (cm <sup>3</sup> )	22×22×4.2	22×22×19
Voxel dimensions (mm <sup>3</sup> )	0.93×1.3×7	0.93×0.93×1.9
Temporal resolution (s)	5	5
Injection delay (s)	20	60
Total scan time (min:s)	4:08	5:29
Time frames	50	61
Sampling pattern	Cartesian 3DFT linear order	Cartesian 3DFT golden-angle radial order
Acceleration factor	2×	30×

slices of the high-resolution experimental scan were averaged to match the slice thickness of the conventional scan. Then  $K^{\text{trans}}$  maps were computed using the Patlak analysis<sup>3,45,46</sup> and a population-averaged analytic arterial input function (AIF).<sup>47</sup>

Quantitative evaluation was performed using the  $K^{\text{trans}}$  histogram within radiologist-defined ROI.<sup>15,48–50</sup> Under the guidance of an experienced neuroradiologist (20 yr of experience), tight ROIs were drawn on  $K^{\text{trans}}$  maps to included the highest  $K^{\text{trans}}$  values. The maximum  $K^{\text{trans}}$  values were calculated for both scans and compared.

Qualitative evaluation was performed using radiologists' rating. Two experienced neuroradiologists (10 and 20 yr of experience, respectively) from our institution reviewed and scored the images. For each subject, three types of images were shown for the conventional and experimental scans (a total of six image sets): (1) time-resolved images of one slice through the tumor (three slices averaged in experimental scan), (2) postcontrast-enhanced images (no slice average for experimental scan), and (3) BBB permeability  $K^{\text{trans}}$  maps. Radiologists were blinded to the acquisition type (conventional or experimental), and the presentation order for every scan was randomized. A 4-point Likert scale was used to quantify the general image quality, where 3 = good, 2 = average, 1 = poor, = nondiagnostic

In the second round of qualitative evaluation, the same Neuroradiologists were shown the full resolution conventional and experimental DCE-MRI results and were asked to evaluate three subcategories of image quality: (1) SNR, which incorporates the visual appearance of noise, (2) apparent spatial resolution, which incorporates sharpness of the images, and (3) conspicuity of tumor enhancement, which incorporates the detectability and sensitivity of contrast enhancement in the tumor. For each category, readers were asked to determine if the conventional scan was superior, if the two were equal, or if the experimental scan was superior. Conventional and experimental scan images (postcontrast images, time-resolved images, and  $K^{\text{trans}}$  maps) were shown to the radiologists, who were not blinded to the scan type.

### 3. RESULTS

#### 3.A. Experiment results

Table III contains the demographic and clinical information for the 15 patients who were included in the data analysis. All experimental data sets were reconstructed using the same empirical constraint penalty values [the  $\lambda$ 's in Eq. (1)]. Reconstruction time was roughly 8 h/dataset.

Figure 1 contains typical postcontrast-enhanced DCE-MRI images from two subjects, one with a large 6 cm glioblastoma and the other with multiple metastatic melanoma tumors scattered throughout the entire brain. The experimental approach was able to provide detailed depiction of the entire tumor body and tumor boundary, and capture all the possible small lesions (14 in total) in the whole coverage of the brain (see arrows). The tumor boundary was clearly visualized in any scan plane, and small, scattered lesions were easily identified in coronal/sagittal reformats. Conversely, the conventional scan provided limited spatial coverage (only 4 lesions were

TABLE III. Patient demographic and clinical information of the 15 brain tumor patients participated in the study.

No.	Sex	Age	Symptom	Tumor size (cm) <sup>a</sup>
001	F	46	Glioblastoma	2.4
002	M	71	Glioblastoma	2.3
003	F	76	Meningioma	1.9
004	F	53	Metastasis	3.4
005	M	26	Astrocytoma	1.6
006	M	77	Meningioma	0.8
007	M	72	Metastatic melanoma	1.0
008	M	65	Glioblastoma	6.0
009	M	71	Glioblastoma	1.5
010	F	65	Metastatic ovarian cancer	1.3
011	F	38	Glioblastoma	0.5
012	F	72	Meningioma	1.4
013	F	22	Glioblastoma	2.4
014	F	78	Metastatic melanoma	1.6
015	F	59	Meningioma	3.9

<sup>a</sup>Tumor size was measured by the longest diameter in the postcontrast T1w images.

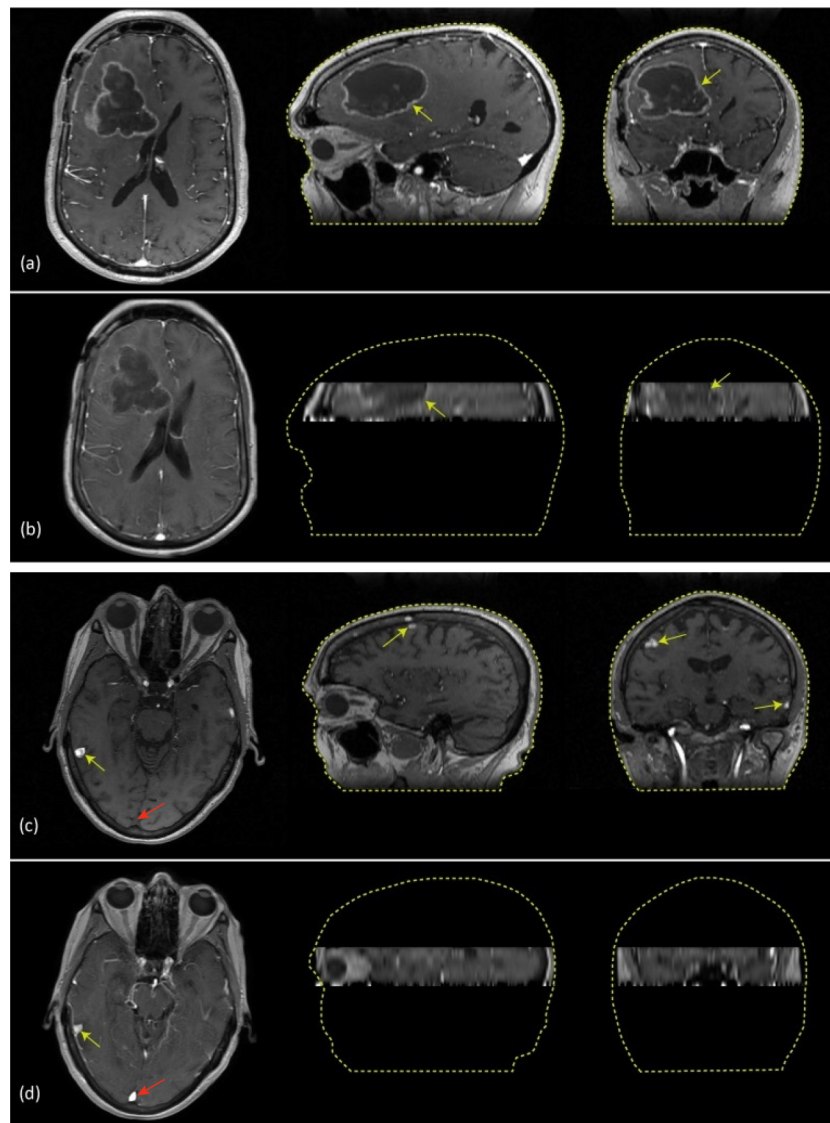


FIG. 1. Final DCE-MRI time frames from two patients illustrating the volume coverage of [(a) and (c)] experimental and [(b) and (d)] conventional scans. (a) and (b): 65/M patient with a 6 cm glioblastoma tumor (subject #008). Experimental scan (a) shows significantly larger coverage than the spatial coverage of the conventional scan (b), where on the sagittal and coronal reformats, only a thin slab of brain can be covered. (c) and (d): 78/F patient with metastatic melanoma (subject #014), only 4 lesions were captured by the clinical scan (d), and all 14 lesions were captured by the experimental scan (c). Note that the conventional scans show bright signal in the sagittal sinus (red arrows) and other blood vessels due to inflow enhancement which are not present in the experimental scans because of the whole-brain coverage. This was consistently observed in all subjects. Only three orthogonal slices are shown here. Postcontrast and time-resolved DCE-MRI videos for case #008 (a) and (b) are available. (Multimedia view) [URL: <http://dx.doi.org/10.1118/1.4944736.1>] [URL: <http://dx.doi.org/10.1118/1.4944736.2>] [URL: <http://dx.doi.org/10.1118/1.4944736.3>] [URL: <http://dx.doi.org/10.1118/1.4944736.4>]

captured), and the sagittal and coronal reformats had extremely low resolution in the slice encoding direction. In all cases, the experimental scan provided clearer and crisper depictions of all lesions that were presented.

Another benefit of whole-brain coverage is that it essentially eliminates inflow enhancement artifacts. Figure 1(c) shows bright signal in the sagittal sinus stemming from inflow enhancement in a conventional scan where only a 6 cm axial slab is imaged. This inflow enhancement was consistently observed in every conventional scan and is strongest in slices at the edge of the imaging slab. In contrast, Fig. 1(d) shows that inflow enhancement was not present in the experimental scans.

Figure 2 demonstrates registered anatomic images and  $K^{\text{trans}}$  maps from two other representative patients, with conventional-then-experimental and experimental-then-conventional protocols, respectively. Note that the experimental images were blurred in the slice-encoding direction to match the conventional protocol. Anatomic images yielded similar quality in the regions of interest.  $K^{\text{trans}}$  measurements from the second scan were consistently 42%–66% of that from the first scan in the ROI of the tumor, regardless of the scan order. The  $K^{\text{trans}}$  maps, despite intensity differences (due to scan order), provided comparable information and superior image quality based on the radiologists' ratings, described below.

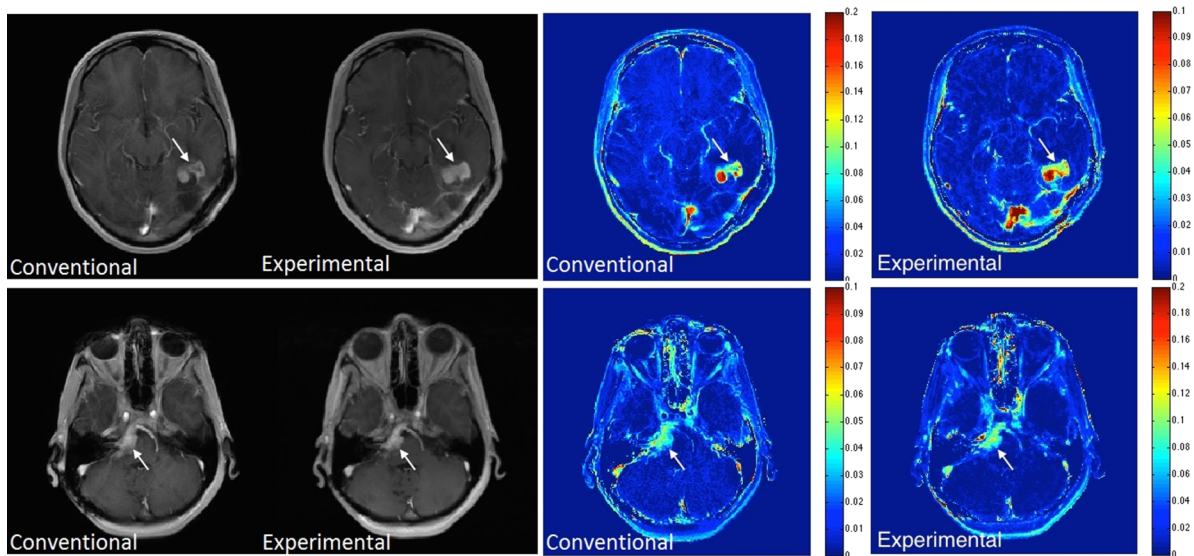


FIG. 2. Registered anatomic images and  $K^{trans}$  maps from two other representative patients. On the left are the registered anatomic images; on the right are  $K^{trans}$  maps. The top row is from patient #013 with a glioblastoma (see arrows) using conventional-then-experimental protocol. The bottom row is from patient #015 with a meningioma (see arrows) using experimental-then-conventional protocol. Both sets of anatomical images provide comparable features and image quality, and the  $K^{trans}$  maps convey comparable diagnostic information despite intensity differences.

**3.B. Quantitative assessment**

Figure 3 shows a scatter plot of the maximum  $K^{trans}$  value within manually segmented tumor ROIs between two DCE-MRI scans. Each pair of scans was performed using one of three possible orderings: conventional-then-experimental (blue circle), experimental-then-conventional (green diamond), and double conventional (red star, see Appendix B). Although the second scan underestimates  $K^{trans}$ , the two measurements were still highly correlated with correlation coefficient  $r = 0.513$ . The mean difference between the two scans was 0.036, which corresponds to a consistent negative bias consistent with contrast residue from the previous injection.

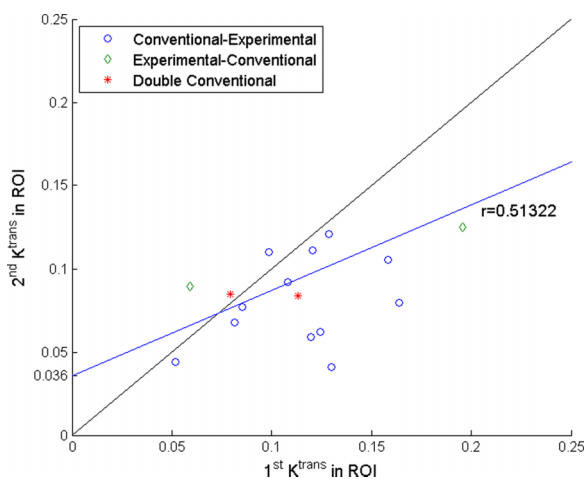


FIG. 3. Scatter plot of the maximum  $K^{trans}$  in tumor ROIs for the first and second DCE-MRI scans. Conventional-then-experimental (13 cases), experimental-then-conventional (2 cases), and double conventional (2 cases, see Appendix B) are all shown. The correlation coefficient was 0.5132. The second scan experienced a consistent underestimation of  $K^{trans}$  due to contrast residue (see Appendix B).

**3.C. Qualitative assessment**

Table IV lists the two radiologists’ ratings of the images. The Likert scale scores of overall image quality were averaged across image types and were shown for all 15 patients. The three subcategories, SNR, apparent resolution, and conspicuity of tumor enhancement, were shown as experimental-better (denoted by “+”), scans are equal (denoted by “=”), or conventional-better (denoted by “-”). Both radiologists consistently rated the experimental scans as higher or equal in quality to the conventional scans in terms of SNR, effective resolution, and fine details. The conventional scan was not deemed superior to the experimental scan in any of the cases by either radiologists. The radiologists also indicated that they observed “better white/gray matter contrast,” “improved resolution and edge sharpness,” “reduced phase-encoding artifacts,” “reduced noise level,” and “better detection of tumor with large coverage of the brain,” from the experimental scan images.

Histograms of the Likert scores for both conventional and experimental scans are shown in Fig. 4. The scores for the three image types were combined to show the overall performance of conventional and experimental scans. Qualitative evaluation from the experimental scans (mostly 2 and 3) clearly outperformed that of the conventional scans (mostly 1).

**4. DISCUSSION**

We have implemented a prospective undersampling and constrained reconstruction scheme for high-resolution whole-brain DCE-MRI. We have performed a pilot comparison study in fifteen brain tumor patients which has demonstrated the strength of this technique and its potential impact on clinical DCE-MRI.

Specifically, we have shown that the DCE-MRI with constrained reconstruction is able to provide much higher

TABLE IV. Two radiologists' scores across the 15 patients for conventional and experimental DCE-MRI scans. A 4-point Likert scale was used to score the overall image quality (3 = good, 2 = average, 1 = poor, 0 = nondiagnostic), and the average of this score was taken for each patient across the three image types. Three subcategories of image quality (SNR, apparent resolution, conspicuity of tumor enhancement) were scored as follows: +: experimental-better, =: equal, -: conventional-better (I: Radiologist 1. II: Radiologist 2).

NO.	Average Likert score				SNR		Resolution		Conspicuity	
	Conventional		Experimental		I	II	I	II	I	II
	I	II	I	II						
1	1	1.67	2	1	+	+	+	+	+	+
2	1	1	2.33	1.67	+	+	=	+	+	+
3	1	1	2	1.67	+	+	+	+	=	+
4	1.67	1.33	2.67	1.67	+	+	+	+	=	+
5	1	1.33	2.33	1.67	+	+	+	+	=	+
6	1.33	1	2.67	2	+	+	+	+	=	+
7	1	2.33	3	2	=	=	=	+	+	+
8	1	1.33	3	2.33	+	+	+	+	+	+
9	1	1.67	2.33	2	+	+	=	+	+	+
10	1	1.33	2.33	1.33	+	+	=	+	=	+
11	1	1.33	3	2	+	+	+	+	=	+
12	1	1.33	3	2	+	+	+	+	=	+
13	1	1	3	2.67	+	+	+	+	=	+
14	1	1	3	2	+	+	+	+	=	+
15	1	0.67	2	2	+	=	+	+	=	=

spatiotemporal resolution and whole-brain spatial coverage compared to current DCE-MRI methods. This is extremely important when imaging large tumors or patients with multiple metastatic lesions, which the conventional scans fail to completely capture due to poor coverage and/or low spatial resolution. Within the same ROI of the conventional scan, radiologists' reported improved quality, comparable or better diagnostic information in both anatomic images and  $K^{trans}$  maps of the experimental scan.

The experimental images show better SNR, resolution, and lesion conspicuity, as well as overall image quality score, despite significant undersampling. This is due to novelty in the way that raw data are reconstructed. In the conventional scan, each time frame is reconstructed independent of every

other time frame. In the experimental scan, each time frame is undersampled in  $k$ -space, but all time frames are reconstructed in a single step and the mutual information between time points is leveraged through the use of temporal constraints. This is precisely the reason that compressed sensing and constrained reconstruction methods can achieve high acceleration factors with equivalent or superior image quality, despite undersampling each time frame. In DCE-MRI (and similarly, time-resolved MR angiography), rapid temporal changes are limited to spatial positions containing vessels, and temporal changes elsewhere are smooth. This makes the images sparse after a temporal finite difference or high pass filter operator is applied. The experimental method leverages information from several time points, which boosts the effective signal-to-noise ratio and image quality, even at high acceleration rates. Regularization of this kind, with spatial and temporal constraints, is common in image and video denoising applications not limited to MRI.<sup>51-53</sup>

The use of sparsity constraints during image reconstruction often has unwanted side effects. For instance, spatial wavelet constraints can produce image blurring and loss of fine details, and temporal finite difference constraints can produce temporal stair-stepping artifacts. This work builds on prior work,<sup>33</sup> which found that these side effects were mitigated by using multiple sparsity constraints, rather than relying on just one.

In a typical clinical protocol, conventional high-resolution whole-brain 3D T1-weighted static image volumes were acquired before the GBCA injection and near the end of the exam, following all GBCA administration. It is worth noting that the first and last time frames of the experimental high-resolution whole-brain DCE scan also constitute precontrast- and postcontrast-enhanced T1-weighted images. This could

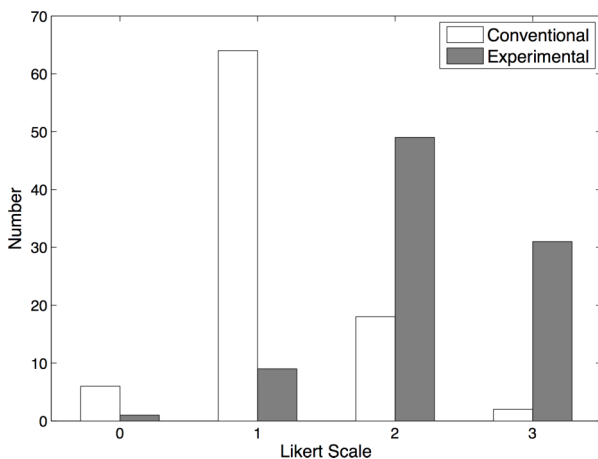


FIG. 4. Histogram of all conventional and experimental scores combining the three image types. The statistics of conventional and experimental scans are  $1.2 \pm 0.6$  and  $2.2 \pm 0.7$ , respectively.



enable the experimental scan to take place of additional static precontrast- and postcontrast-enhanced image acquisitions, saving scan resources and time.

There are several factors that preclude an optimal comparison with the conventional protocol. First, both conventional and experimental scans were performed in the same session with a relatively short interval. The rationale for this was practicality. Brain tumor patients were unwilling to come back on another day for a second MRI scan that was purely for research purposes. The consequence is that there is significant residual GBCA on board prior to the second DCE MRI scan, which could lead to underestimation of  $K^{\text{trans}}$  values in the second scan. The order of conventional and experimental scans was reversed in the last two cases, and the same  $K^{\text{trans}}$  underestimation was observed in the second scan, consistent with residual GBCA (not the imaging technique) being the cause. Please see Appendix B for details including an experimental verification. Additionally, due to the short interval between the two scans, tumors that take up contrast slowly may show higher conspicuity on the second scan due to temporal order (e.g., Fig. 2, top row). A limitation of this study is that only two cases were performed with the experimental-then-conventional order. In both cases, the experimental (first) scan was rated as having higher tumor conspicuity than the conventional (second) scan, but this should be considered anecdotal because of the small sample size.

Another limiting factor for constrained reconstruction is the high computational complexity. Using a powerful workstation and an efficient MATLAB implementation, data reconstruction per dataset required 8 h at the time the studies were performed. Since then, we have been able to shorten the reconstruction time to 1.5 h by incorporating coil compression,<sup>54</sup> reduced temporal segmentation, and optimization of the MATLAB implementation. In general, reconstruction time is a limitation for iterative constrained reconstruction techniques, making them problematic for real-time imaging or applications that require immediate availability of image data. Parallelization, GPU based computation, and efficient c-based implementation are being explored by many groups, and these have provided reconstruction speedup on the order of 3–200.<sup>17,55</sup>

This study did not include a quantitative assessment of spatial and contrast resolution, and this remains an important next step in the evaluation of constrained reconstruction techniques in DCE-MRI. Because the experimental method involves nonlinear reconstruction, the definition of true spatial and contrast resolution is nontrivial and is an open research question. Partial solutions such as characterization of local point spread functions<sup>56</sup> and validation with digital or physical reference objects<sup>57</sup> exist but require dedicated investigation and are highly object-dependent. There are efforts underway to develop anatomically realistic brain DCE-MRI digital reference objects,<sup>58,59</sup> which will facilitate such work.

Under sampling and constrained reconstruction for MRI are rapidly developing areas. Several groups, including ours, are developing constraints and quality evaluation techniques to maximize the reconstruction quality. The constraints used in this study have been previously validated in a retrospective study,<sup>33</sup> and the prospective study results shown here further

demonstrate the application and feasibility of constrained reconstruction for clinical DCE-MRI.

## 5. CONCLUSION

We conclude that high-resolution whole-brain DCE-MRI using constrained reconstruction is clinically feasible and provides superior image quality compared to the current conventional DCE-MRI technique. In our study, the experimental approach provided superior image and pharmacokinetic map quality without compromising diagnostic information compared to the current DCE-MRI approach. The experimental approach also provided complete characterization of all normal and abnormal tissues, and allowed for arbitrary multiplanar reformatting of data. This was a significant advantage in two of the fifteen cases, one with a large glioblastoma multiforme that exceeded the spatial coverage of the conventional scan and had a narrow enhancing margin and the other with 14 metastatic lesions of which only 4 were characterized by the conventional scan. This study represents, to the best of our knowledge, the first prospective evaluation of brain DCE-MRI with constrained reconstruction. Compared to current best practices, this new approach has the potential to vastly improve visualization and characterization of brain lesions with DCE-MRI.

## ACKNOWLEDGMENTS

The authors would like to thank Dr. Samuel Barnes and Dr. Angel Pineda for useful discussions related to DCE pharmacokinetic modeling and image quality evaluation, respectively. The authors also thank Mario Franco and Samuel Valencerina for helping in recruiting and scanning brain tumor patients. Research reported in this publication was partially supported by the National Center for Advancing Translational Sciences of the National Institutes of Health under Award No. UL1TR000130 (formerly by the National Center for Research Resources, Award No. UL1RR031986). The content is solely the responsibility of the authors and does not necessarily represent the official views of the National Institutes of Health. M.S.S. was supported in part by SC CTSI (NIH/NCRR/NCATS) Grant No. KL2TR000131.

## APPENDIX A: RECONSTRUCTION ALGORITHM

To solve the  $\ell_1$ -norm constrained optimization problem from Eq. (1), we used ADMM, a version of augmented Lagrangian methods.<sup>39</sup> All sparsity transforms can be denoted by a tall matrix  $T$ , that is,  $T = [V, TV, \Psi]^T$ . Dummy variables  $u$ ,  $v$  are used to split Eq. (1) to Eq. (A1), where  $\lambda$  is a long vector that has  $\lambda_1, \lambda_2$ , and  $\lambda_3$  in the corresponding transform location,

$$\min_{u,v} \|y - F_u u\|_2^2 + \lambda \|v\|_1 \text{ s.t. } v = Tx, u = Sx. \quad (\text{A1})$$

Then Lagrangian method is used to convert Eq. (A1) to an unconstrained problem in the following:

$$\min_{u,v,x,e_1,e_2} \|y - F_u u\|_2^2 + \lambda \|v\|_1 + \rho_1 \|Tx - v - e_1\|_2^2 + \rho_2 \|Sx - u - e_2\|_2^2, \quad (\text{A2})$$

where  $e_1, e_2$  are Lagrange multiplier terms, and  $\rho_1, \rho_2$  are penalties for the axillary dummy variables. With the Lagrange terms ( $e_1, e_2$ ), the penalty parameters ( $\rho_1, \rho_2$ ) need not tend to large values for the equivalence of Eqs. (A2) and (A1) to hold; the value of these parameters does not affect the final solution, just the rate of convergence. We empirically chose them to be 0.05.

Denoting the objective function in Eq. (A2) as  $L(x, u, v)$ , the problem can be decoupled to simpler well-defined subproblems, where every subproblem takes an analytical form, and can be solved in a single step. The algorithm relies on iterating between these subproblems until convergence to a guaranteed global minimum. The steps are as follows.

Initialization :

Select  $x^0, u^0 = Sx^0, v^0 = Tx^0$ , and  $n = 0$

Repeat :

$$x^{n+1} = \underset{x}{\operatorname{argmin}} L(x, v^n, u^n)$$

$$= [\rho_2 S' S + \rho_1 T' T]^{-1} (\rho_2 S'(u^n + e_2^n) + \rho_3 T'(v^n + e_3^n))$$

$$u^{n+1} = \underset{u}{\operatorname{argmin}} L(x^{n+1}, v^n, u)$$

$$= [F'_u F_u + \rho_2 S' S]^{-1} (F'_u y + \rho_2 (Sx^{n+1} - e_2^n))$$

$$v^{n+1} = \underset{v}{\operatorname{argmin}} L(x^{n+1}, v, u^{n+1}) = \operatorname{shrink}(Tx^{n+1} - e_1^n; \lambda/\rho_1)$$

$$e_1^{n+1} = e_1^n + (v^{n+1} - Tx^{n+1})$$

$$e_2^{n+1} = e_2^n + (u^{n+1} - Sx^{n+1})$$

$$n = n + 1$$

Until stopping criterion is met

Note that  $S'S = I$  because of the properties of the sensitivity maps, the above steps were simplified into 5 steps compared to 7 steps in Ref. 39, which accelerated the reconstruction and simplified the workflow.

## APPENDIX B: DOUBLE INJECTION

In this study, a Patlak model was used to estimate PK parameters for conventional and experimental scans. The following equation shows the fitting of  $K^{\text{trans}}$  and  $v_p$  from

contrast concentration curves of plasma  $C_p(t)$  and tissue  $C_t(t)$ :

$$\Delta C_t(t) = K^{\text{trans}} \int_0^t C_p(\tau) d\tau + v_p C_p(t), \tag{B1}$$

$C_p(t)$  is the AIF, where we used a population-based analytic form,<sup>47</sup> and  $\Delta C_t(t)$  is the GBCA concentration change in the tissue, which is derived from the signal intensity in the dynamic images.  $K^{\text{trans}}$  is the volume transfer constant and  $v_p$  is the fractional plasma volume.

The Patlak model is used because it is robust to noise, in part due to its simplicity and the dependence on linear (vs nonlinear) estimation.<sup>46,60</sup> The model is based on the assumption that there is no backflux from the interstitium during a short scan.<sup>46</sup> This assumption is not satisfied for the second injection in which residual GBCA in the interstitium from the first scan causes backflux that cannot be ignored. Use of this model causes underestimation of  $K^{\text{trans}}$  values for the second scan, as we illustrate below using simulations.

The double-injection experiment is simulated using the more accurate two-compartment exchange model (2CXM). Figure 5(a) shows simulated  $C_p(t)$  and  $C_t(t)$  with 20 min separation between injections. Figure 5(b) shows the simulated  $\Delta C_t(t)$  from first and second injections, where the arrows indicate the altered curve due to residual GBCA. This residual, indicated with yellow circles in Figure 5(a), is directly related to the extracellular extravascular volume fraction and the GBCA concentration in the extracellular extravascular space prior to the second injection. The end result is 16%–50% underestimation of  $K^{\text{trans}}$  for the second scan. This projected range is based on PK parameter values reported in the literature for brain tumor.<sup>60</sup> Figure 5(c) shows measured  $\Delta C_t(t)$  curves from a representative tumor voxel in one case in our study.

To further determine if this underestimation is caused by injection order, we performed experiments in three brain tumor patients, where the conventional DCE-MRI scan was performed twice in a single session. In the three subjects, tumor  $K^{\text{trans}}$  was underestimated in the second scan by 15%, 0%, and 24%. We consider these data to be anecdotal, but consistent with the simulations and the observed underestimation in the second scan of the conventional-then-experimental and experimental-then-conventional patient scans. Figures 6(a)–6(d) contain zoomed anatomic

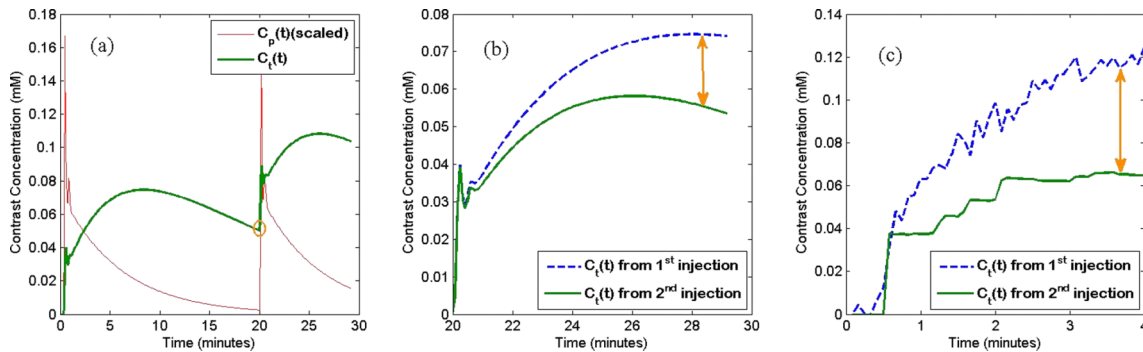


FIG. 5. (a) The 2CXM simulated contrast concentration curves  $C_p(t)$  (scaled by 0.2x) and  $C_t(t)$  for double injections, separated by 20 min. (b)  $\Delta C_t(t)$  calculated from the first and second injections, where  $\Delta C_t(t)$  from the second injection is lower primarily due to high backflux from the tissue to the plasma. (c) Actual measured  $\Delta C_t(t)$  curves in one tumor voxel from a representative patient data, which matched the trend of the simulation.

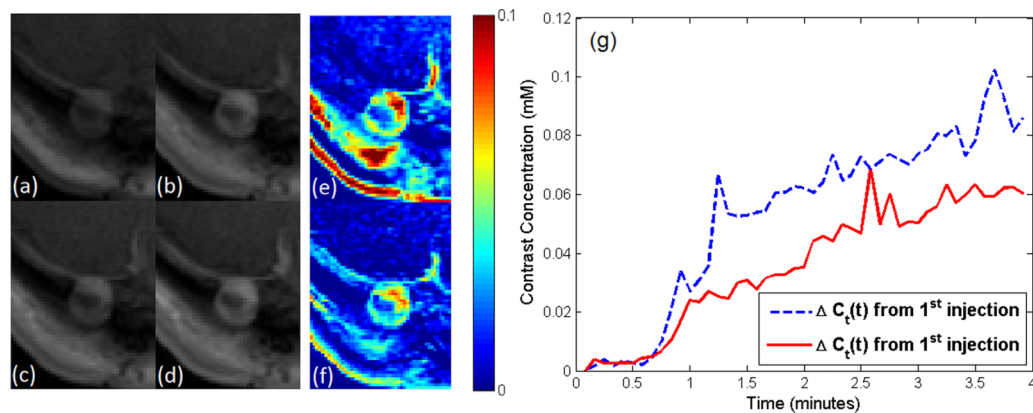


FIG. 6. (a) and (b): Precontrast and postcontrast images of first conventional DCE scan, cropped around an enhancing tumor. (c) and (d): Precontrast and postcontrast images from the second conventional DCE scan. (e):  $K^{\text{trans}}$  maps from first DCE scan, (f):  $K^{\text{trans}}$  maps from second DCE scan. (g): Measured  $\Delta C_t(t)$  curves in the tumor ROI for the two conventional scans.

images from the 24% case before and after contrast injection for the two scans, where contrast residue can be seen in the second scan. Figures 6(e) and 6(f) contain zoomed  $K^{\text{trans}}$  maps, where the second scan produced lower estimated  $K^{\text{trans}}$  compared to the first scan. In this case, the mean  $K^{\text{trans}}$  values in tumor ROI from the second scan were 24% lower than the first scan. Figure 6(g) shows measured  $\Delta C_t(t)$  curves in these two conventional scans, which matches the trend observed in simulations, conventional-then-experimental scans, and experimental-then-conventional scans.

barrier breakdown in the aging human report blood-brain barrier breakdown in the aging human hippocampus," *Neuron* **85**(2), 296–302 (2015).

<sup>4</sup>Author to whom correspondence should be addressed. Electronic mail: yiguo@usc.edu; Telephone: (213) 572-7827; Fax: (213) 740-4651.

<sup>1</sup>A. K. Heye, R. D. Culling, C. V. Hernández, M. J. Thrippleton, and J. M. Wardlaw, "Assessment of blood–Brain barrier disruption using dynamic contrast-enhanced MRI. A systematic review," *NeuroImage: Clin.* **6**, 262–274 (2014).

<sup>2</sup>J. P. B. O'Connor, A. Jackson, G. J. M. Parker, C. Roberts, and G. C. Jayson, "Dynamic contrast-enhanced MRI in clinical trials of antivascular therapies," *Nat. Rev. Clin. Oncol.* **9**(3), 167–177 (2012).

<sup>3</sup>P. S. Tofts and A. G. Kermode, "Measurement of the blood–brain barrier permeability and leakage space using dynamic MR imaging. I. Fundamental concepts," *Magn. Reson. Med.* **17**(2), 357–367 (1991).

<sup>4</sup>P. S. Tofts, G. Brix, D. L. Buckley, J. L. Evelhoch, E. Henderson, M. V. Knopp, H. B. Larsson, T. Y. Lee, and R. M. Weisskoff, "Estimating kinetic parameters from dynamic contrast-enhanced T(1)-weighted MRI of a diffusible tracer: Standardized quantities and symbols," *J. Magn. Reson. Imaging* **10**(3), 223–232 (1999).

<sup>5</sup>H. B. Larsson, M. Stubgaard, J. L. Frederiksen, M. Jensen, O. Henriksen, and O. B. Paulson, "Quantitation of blood-brain barrier defect by magnetic resonance imaging and gadolinium-DTPA in patients with multiple sclerosis and brain tumors," *Magn. Reson. Med.* **16**, 117–131 (1990).

<sup>6</sup>M. Law, S. Yang, J. S. Babb, E. A. Knopp, J. G. Golfinos, D. Zagzag, and G. Johnson, "Comparison of cerebral blood volume and vascular permeability from dynamic susceptibility contrast-enhanced perfusion MR imaging with glioma grade," *Am. J. Neuroradiol.* **25**, 746–755 (2004).

<sup>7</sup>S. Yang, M. Law, D. Zagzag, H. H. Wu, S. Cha, J. G. Golfinos, E. A. Knopp, and G. Johnson, "Dynamic contrast-enhanced perfusion MR imaging measurements of endothelial permeability: Differentiation between atypical and typical meningiomas," *Am. J. Neuroradiol.* **24**(8), 1554–1559 (2003).

<sup>8</sup>S. P. Cramer, H. Simonsen, J. L. Frederiksen, E. Rostrup, and H. B. W. Larsson, "Abnormal blood-brain barrier permeability in normal appearing white matter in multiple sclerosis investigated by MRI," *NeuroImage: Clin.* **4**, 182–189 (2014).

<sup>9</sup>A. Montagne, S. R. Barnes, M. Law, B. V. Zlokovic, A. Montagne, S. R. Barnes, M. D. Sweeney, M. R. Halliday, and H. C. Chui, "Blood-brain

<sup>10</sup>R. H. El Khoulil, K. J. Macura, M. A. Jacobs, T. H. Khalil, I. R. Kamel, A. Dwyer, and D. A. Bluemke, "Dynamic contrast-enhanced MRI of the breast: Quantitative method for kinetic curve type assessment," *Am. J. Roentgenol.* **193**(4), W295–W300 (2009).

<sup>11</sup>A. B. Rosenkrantz, R. P. Lim, M. Haghighi, M. B. Somberg, J. S. Babb, and S. S. Taneja, "Comparison of interreader reproducibility of the prostate imaging reporting and data system and Likert scales for evaluation of multiparametric prostate MRI," *AJR, Am. J. Roentgenol.* **201**(4), W612–W618 (2013).

<sup>12</sup>M. S. Shiroishi, M. Habibi, D. Rajderkar, C. Yurko, J. L. Go, A. Lerner, M. A. Mogensen, P. E. Kim, and M. Law, "Perfusion and permeability MR imaging of gliomas," *Technol. Cancer Res. Treat.* **10**, 59–71 (2011).

<sup>13</sup>M. J. Paldino and D. P. Barboriak, "Fundamentals of quantitative dynamic contrast-enhanced MR imaging," *Magn. Reson. Imaging Clin. North Am.* **17**, 277–289 (2009).

<sup>14</sup>J. C. Miller, H. H. Pien, D. Sahani, A. G. Sorensen, and J. H. Thrall, "Imaging angiogenesis: Applications and potential for drug development," *J. Natl. Cancer Inst.* **97**, 172–187 (2005).

<sup>15</sup>A. A. Thomas, J. Arevalo-Perez, T. Kaley, J. Lyo, K. K. Peck, W. Shi, Z. Zhang, and R. J. Young, "Dynamic contrast enhanced T1 MRI perfusion differentiates pseudoprogression from recurrent glioblastoma," *J. Neuro-Oncol.* **125**(1), 183–190 (2015).

<sup>16</sup>S. P. Cramer and H. B. W. Larsson, "Accurate determination of blood-brain barrier permeability using dynamic contrast-enhanced T1-weighted MRI: A simulation and *in vivo* study on healthy subjects and multiple sclerosis patients," *J. Cereb. Blood Flow Metab.* **34**, 1655–1665 (2014).

<sup>17</sup>A. B. Rosenkrantz, C. Geppert, R. Grimm, T. K. Block, C. Glielmi, L. Feng, R. Otazo, J. M. Ream, and H. Chandarana, "Dynamic contrast-enhanced MRI of the prostate with high spatiotemporal resolution using compressed sensing, parallel imaging, and continuous golden-angle radial sampling: Preliminary experience," *J. Magn. Reson. Imaging* **41**, 1365–1373 (2015).

<sup>18</sup>M. Lustig, D. Donoho, and J. M. Pauly, "Sparse MRI: The application of compressed sensing for rapid MR imaging," *Magn. Reson. Med.* **58**(6), 1182–1195 (2007).

<sup>19</sup>S. P. Awate and E. V. R. DiBella, "Spatiotemporal dictionary learning for undersampled dynamic MRI reconstruction via joint frame-based and dictionary-based sparsity," *9th IEEE International Symposium on Biomedical Imaging (IEEE, ISBI, 2012)*, pp. 318–321.

<sup>20</sup>J. Caballero, A. N. Price, D. Rueckert, and J. V. Hajnal, "Dictionary learning and time sparsity for dynamic MR data reconstruction," *IEEE Trans. Med. Imaging* **33**(4), 979–994 (2014).

<sup>21</sup>U. Gamper, P. Boesiger, and S. Kozerke, "Compressed sensing in dynamic MRI," *Magn. Reson. Med.* **59**(2), 365–373 (2008).

<sup>22</sup>H. Jung, K. Sung, K. S. Nayak, E. Y. Kim, and J. C. Ye, "k-t FOCUSS: A general compressed sensing framework for high resolution dynamic MRI," *Magn. Reson. Med.* **61**(1), 103–116 (2009).

<sup>23</sup>K. P. Pruessmann, M. Weiger, M. B. Scheidegger, and P. Boesiger, "SENSE: Sensitivity encoding for fast MRI," *Magn. Reson. Med.* **42**(5), 952–962 (1999).

- <sup>24</sup>M. Lustig and J. M. Pauly, "SPIRiT: Iterative self-consistent parallel imaging reconstruction from arbitrary k-space," *Magn. Reson. Med.* **64**(2), 457–471 (2010).
- <sup>25</sup>M. Uecker, P. Lai, M. J. Murphy, P. Virtue, M. Elad, J. M. Pauly, S. S. Vasanawala, and M. Lustig, "ESPIRiT—An eigenvalue approach to auto-calibrating parallel MRI: Where SENSE meets GRAPPA," *Magn. Reson. Med.* **71**, 990–1001 (2014).
- <sup>26</sup>L. Feng, R. Grimm, K. T. Block, H. Chandarana, S. Kim, J. Xu, L. Axel, D. K. Sodickson, and R. Otazo, "Golden-angle radial sparse parallel MRI: Combination of compressed sensing, parallel imaging, and golden-angle radial sampling for fast and flexible dynamic volumetric MRI," *Magn. Reson. Med.* **72**(1), 707–717 (2014).
- <sup>27</sup>T. Zhang, J. Y. Cheng, A. G. Potnick, R. A. Barth, M. T. Alley, M. Uecker, M. Lustig, J. M. Pauly, and S. S. Vasanawala, "Fast pediatric 3D free-breathing abdominal dynamic contrast enhanced MRI with high spatiotemporal resolution," *J. Magn. Reson. Imaging* **41**(2), 460–473 (2015).
- <sup>28</sup>H. Wang, Y. Miao, K. Zhou, Y. Yu, S. Bao, Q. He, Y. Dai, S. Y. Xuan, and J. Hu, "Feasibility of high temporal resolution breast DCE-MRI using compressed sensing theory," *Med. Phys.* **37**(9), 4971–4981 (2010).
- <sup>29</sup>A. V. Barger, W. F. Block, Y. Toropov, T. M. Grist, and C. A. Mistretta, "Time-resolved contrast-enhanced imaging with isotropic resolution and broad coverage using an undersampled 3D projection trajectory," *Magn. Reson. Med.* **48**(2), 297–305 (2002).
- <sup>30</sup>C. R. Haider, H. H. Hu, N. G. Campeau, J. Huston, and S. J. Riederer, "3D high temporal and spatial resolution contrast-enhanced MR angiography of the whole brain," *Magn. Reson. Med.* **60**(3), 749–760 (2008).
- <sup>31</sup>J. D. Trzasko, C. R. Haider, E. A. Borisch, N. G. Campeau, J. F. Glockner, S. J. Riederer, and A. Manduca, "Sparse-CAPR: Highly accelerated 4D CE-MRA with parallel imaging and nonconvex compressive sensing," *Magn. Reson. Med.* **66**(4), 1019–1032 (2011).
- <sup>32</sup>G. R. Lee, N. Seiberlich, J. L. Sunshine, T. J. Carroll, and M. A. Griswold, "Rapid time-resolved magnetic resonance angiography via a multiecho radial trajectory and GraDeS reconstruction," *Magn. Reson. Med.* **69**(2), 346–359 (2013).
- <sup>33</sup>R. M. Lebel, J. Jones, J.-C. Ferre, M. Law, and K. S. Nayak, "Highly accelerated dynamic contrast enhanced imaging," *Magn. Reson. Med.* **71**, 635–644 (2014).
- <sup>34</sup>S. Winkelmann, T. Schaeffter, T. Koehler, H. Eggers, and O. Doessel, "An optimal radial profile order based on the golden ratio for time-resolved MRI," *IEEE Trans. Med. Imaging* **26**(1), 68–76 (2007).
- <sup>35</sup>M. Doneva, C. Stehning, K. Nehrke, and P. Börner, "Improving scan efficiency of respiratory gated imaging using compressed sensing with 3D Cartesian golden angle sampling," in *ISMRM* (Proc. ISMRM, 2011), Vol. 19, p. 641.
- <sup>36</sup>Y. Zhu, Y. Guo, R. M. Lebel, M. Law, and K. S. Nayak, "Randomized golden ratio sampling for highly accelerated dynamic imaging," in *ISMRM* (Proc. ISMRM, 2014), Vol. 22, p. 4365.
- <sup>37</sup>S. C. L. Deoni, "High-resolution T1 mapping of the brain at 3T with driven equilibrium single pulse observation of T1 with high-speed incorporation of RF field inhomogeneities (DESPO1-HIFI)," *J. Magn. Reson. Imaging* **26**(4), 1106–1111 (2007).
- <sup>38</sup>Y. Zhu, Y. Guo, S. G. Lingala, R. Marc Lebel, M. Law, and K. S. Nayak, "GOCART: Golden-angle Cartesian randomized time-resolved 3D MRI," *Magn. Reson. Imaging* (2015).
- <sup>39</sup>S. Ramani and J. Fessler, "Parallel MR image reconstruction using augmented Lagrangian methods," *IEEE Trans. Med. Imaging* **30**(3), 694–706 (2011).
- <sup>40</sup>M. V. Afonso, J. M. Bioucas-Dias, and M. A. T. Figueiredo, "Fast image recovery using variable splitting and constrained optimization," *IEEE Trans. Image Process.* **19**(9), 2345–2356 (2010).
- <sup>41</sup>M. V. Afonso, J. M. Bioucas-Dias, and M. A. T. Figueiredo, "An augmented Lagrangian approach to the constrained optimization formulation of imaging inverse problems," *IEEE Trans. Image Process.* **20**(3), 681–695 (2011).
- <sup>42</sup>P. C. Hansen and D. Prost O'Leary, "The use of the l-curve in the regularization of discrete ill-posed problems," *SIAM J. Sci. Comput.* **14**(6), 1487–1503 (1993).
- <sup>43</sup>N. U. Lin, E. Q. Lee, H. Aoyama, I. J. Barani, D. P. Barboriak, B. G. Baumert, M. Bendszus, P. D. Brown, and P. Y. Wen, "Response assessment criteria for brain metastases: Proposal from the RANO group," *Lancet Oncol.* **16**(6), e270–e278 (2015).
- <sup>44</sup>B. M. Ellingson, M. Bendszus, J. Boxerman, D. Barboriak, B. J. Erickson, M. Smits, S. J. Nelson, E. Gerstner, and D. Development, "Consensus recommendations for a standardized brain tumor imaging protocol in clinical trials," *Neuro. Oncol.* **17**, 1188–1198 (2015).
- <sup>45</sup>J. R. Ewing, R. A. Knight, T. N. Nagaraja, J. S. Yee, V. Nagesh, P. A. Whitton, L. Li, and J. D. Fenstermacher, "Patlak plots of Gd-DTPA MRI data yield blood-brain transfer constants concordant with those of <sup>14</sup>C-sucrose in areas of blood-brain opening," *Magn. Reson. Med.* **50**, 283–292 (2003).
- <sup>46</sup>S. P. Sourbron and D. L. Buckley, "Classic models for dynamic contrast-enhanced MRI," *NMR Biomed.* **26**(8), 1004–1027 (2013).
- <sup>47</sup>G. J. M. Parker, C. Roberts, A. Macdonald, G. A. Buonaccorsi, S. Cheung, D. L. Buckley, A. Jackson, Y. Watson, and G. C. Jayson, "Experimentally-derived functional form for a population-averaged high-temporal-resolution arterial input function for dynamic contrast-enhanced MRI," *Magn. Reson. Med.* **56**(5), 993–1000 (2006).
- <sup>48</sup>T. J. Yun, C. K. Park, T. M. Kim, S. H. Lee, J. H. Kim, C. H. Sohn, S. H. Park, I. H. Kim, and S. H. Choi, "Glioblastoma treated with concurrent radiation therapy and temozolomide chemotherapy: Differentiation of true progression from pseudoprogression with quantitative dynamic contrast-enhanced MR imaging," *Radiology* **274**(3), 830–840 (2015).
- <sup>49</sup>P. Kickingereder, B. Wiestler, M. Graf, S. Heiland, H. P. Schlemmer, W. Wick, A. Wick, M. Bendszus, and A. Radbruch, "Evaluation of dynamic contrast-enhanced MRI derived microvascular permeability in recurrent glioblastoma treated with bevacizumab," *J. Neuro-Oncol.* **121**(2), 373–380 (2015).
- <sup>50</sup>D. Bonekamp, K. Deike, B. Wiestler, W. Wick, M. Bendszus, A. Radbruch, and S. Heiland, "Association of overall survival in patients with newly diagnosed glioblastoma with contrast-enhanced perfusion MRI: Comparison of intraindividually matched T1- and T2\* -based bolus techniques," *J. Magn. Reson. Imaging* **42**, 87–96 (2014).
- <sup>51</sup>S. G. Chang, B. Yu, and M. Vetterli, "Adaptive wavelet thresholding for image denoising and compression," *IEEE Trans. Image Process.* **9**(9), 1532–1546 (2000).
- <sup>52</sup>M. Elad and M. Aharon, "Image denoising via sparse and redundant representations over learned dictionaries," *IEEE Trans. Image Process.* **15**(12), 3736–3745 (2006).
- <sup>53</sup>S. H. Chan, R. Khoshabeh, K. B. Gibson, P. E. Gill, and T. Q. Nguyen, "An augmented Lagrangian method for total variation video restoration," *IEEE Trans. Image Process.* **20**(11), 3097–3111 (2011).
- <sup>54</sup>T. Zhang, J. M. Pauly, S. S. Vasanawala, and M. Lustig, "Coil compression for accelerated imaging with Cartesian sampling," *Magn. Reson. Med.* **69**(2), 571–582 (2013).
- <sup>55</sup>J. Gai, N. Obeid, J. L. Holtrop, X.-L. Wu, F. Lam, M. Fu, J. P. Hal-dar, W.-M. Hwu, and B. P. Sutton, "More IMPATIENT: A gridding-accelerated Toeplitz-based strategy for non-Cartesian high-resolution 3D MRI on GPUs," *J. Parallel Distrib. Comput.* **73**(5), 686–697 (2013).
- <sup>56</sup>J. Frahm, S. Schätz, M. Untenberger, S. Zhang, D. Voit, K. D. Merboldt, J. M. Sohns, J. Lotz, and M. Uecker, "On the temporal fidelity of nonlinear inverse reconstructions for real-time MRI—The motion challenge," *Open Med. Imaging J.* **8**, 1–7 (2014).
- <sup>57</sup>T. Wech, D. Stab, J. C. Budich, A. Fischer, J. Tran-Gia, D. Hahn, and H. Kostler, "Resolution evaluation of MR images reconstructed by iterative thresholding algorithms for compressed sensing," *Med. Phys.* **39**(7), 4328–4338 (2012).
- <sup>58</sup>Y. Zhu, Y. Guo, S. G. Lingala, S. Barnes, R. M. Lebel, M. Law, and K. S. Nayak, "Evaluation of DCE-MRI data sampling, reconstruction and model fitting using digital brain phantom," in *ISMRM* (Proc. ISMRM, 2015), Vol. 23, p. 3070.
- <sup>59</sup>R. J. Bosca and E. F. Jackson, "An extensible methodology for creating realistic anthropomorphic digital phantoms for quantitative imaging algorithm comparisons and validation," in *ISMRM* (Proc. ISMRM, 2015), Vol. 23, p. 797.
- <sup>60</sup>S. P. Sourbron and D. L. Buckley, "On the scope and interpretation of the Tofts models for DCE-MRI," *Magn. Reson. Med.* **66**(3), 735–745 (2011).